

**Node-surface and node-line fermions from nonsymmorphic lattice symmetries**Qi-Feng Liang,<sup>1,\*</sup> Jian Zhou,<sup>2</sup> Rui Yu,<sup>3</sup> Zhi Wang,<sup>4</sup> and Hongming Weng<sup>5,6,†</sup><sup>1</sup>*Department of Physics, Shaoxing University, Shaoxing 312000, China*<sup>2</sup>*Department of Materials, Nanjing University, Nanjing 210093, China*<sup>3</sup>*Department of Physics, Harbin Institute of Technology, Harbin 150001, China*<sup>4</sup>*School of Physics and Engineering, Sun Yat-sen University, Guangzhou 510275, China*<sup>5</sup>*Beijing National Laboratory for Condensed Matter Physics, and Institute of Physics, Chinese Academy of Sciences, Beijing 100190, China*<sup>6</sup>*Collaborative Innovation Center of Quantum Matter, Beijing 100190, China*

(Received 2 January 2016; published 18 February 2016)

We propose a kind of topological quantum state of semimetals in the quasi-one-dimensional (1D) crystal family  $BaMX_3$  ( $M = V, Nb, \text{ or } Ta$ ;  $X = S \text{ or } Se$ ) by using symmetry analysis and first-principles calculation. We find that in  $BaVS_3$  the valence and conduction bands are degenerate in the  $k_z = \pi/c$  plane ( $c$  is the lattice constant along the  $\hat{z}$  axis) of the Brillouin zone (BZ). These nodal points form a node surface, and they are protected by a nonsymmorphic crystal symmetry consisting of a twofold rotation about the  $\hat{z}$  axis and a half-translation along the same  $\hat{z}$  axis. The band degeneracy in the node surface is lifted in  $BaTaS_3$  by including strong spin-orbit coupling (SOC) of Ta. The node surface is reduced into 1D node lines along the high-symmetry paths  $k_x = 0$  and  $k_x = \pm\sqrt{3}k_y$  on the  $k_z = \pi/c$  plane. These node lines are robust against SOC and guaranteed by the symmetries of the  $P6_3/mmc$  space group. These node-line states are entirely different from previous proposals which are based on the accidental band touchings. We also propose a useful material design for realizing topological node-surface and node-line semimetals.

DOI: [10.1103/PhysRevB.93.085427](https://doi.org/10.1103/PhysRevB.93.085427)**I. INTRODUCTION**

Searching for new topological states of matter has been an active field since the discovery of topological insulators (TIs) [1,2]. Recently, much attention has been drawn to topological semimetals (TSMs), stimulated by the successful design [3] and experimental observations of Weyl semimetals (WSMs) in transition-metal monophosphides [4,5]. WSMs, first predicted in pyrochlore iridates by Wan *et al.* [6], are topological metallic states in which the Fermi surfaces consist of discrete twofold-degenerate Weyl points. These Weyl points are topologically robust since they carry nontrivial chiral charges. Heikkilä *et al.* have extended the idea of TSMs with Fermi node points to node-line semimetals (NLSs) which host one-dimensional (1D) contacts of conduction and valence bands [7–11]. The node-line fermions have been proposed in realistic materials such as graphene networks [12],  $Cu_3N$  [13],  $Cu_3PdN$  [14], and  $Ca_3P_2$  [15]. Experimental characterization of topological properties of NLSs was carried out for  $PbTaSe_2$  [16]. One of the important topological properties of NLSs is that they support “drumhead”-like flat surface bands [12,17], which may potentially enhance the superconductivity transition temperature [18].

In previous proposals [12–14], ring-like node-line contacts are fragile against spin-orbit coupling (SOC). Including SOC lifts the node-line contacts and drives systems into topological insulators or WSMs. Therefore, searching for stable NLSs robust to SOC [10] is of great interest and importance. Recently, material design principles involving a layer-stacking process of topological insulators and magnetic insulators were given for WSMs [19] and NLSs [17]. Alternatively, in

the present work we provide a route to realize such exotic TSM states by arranging one-dimensional ionic chains in parallel. By using first-principles calculations and symmetry consideration, we show that the quasi-one-dimensional crystal  $BaVS_3$  exhibits a two-dimensional (2D) touching of valence and conduction bands, namely a node surface, at the  $k_z = \pi/c$  plane, with  $c$  being the  $\hat{z}$ -axis lattice constant. In a cousin compound  $BaTaS_3$ , the large SOC of Ta atom lifts the 2D degeneracy and reduces it into 1D node lines which are robust to SOC. The node lines found in the present work are located at the high-symmetry paths  $k_x = 0$  and  $k_x = \pm\sqrt{3}k_y$  on the  $k_z = \pi/c$  plane, demonstrating their purely symmetrical origin, which is different from the accidental-band-degeneracy mechanism of previous node lines [10,16].

The remaining part of this paper is organized as follows. In Sec. II the crystal structure of quasi-1D ionic crystals  $BaMX_3$  ( $M = V, Nb, \text{ or } Ta$ ;  $X = S \text{ or } Se$ ) is presented. Section III is devoted to the materials realization of the node-surface state in  $BaVS_3$  and the NLS in  $BaTaS_3$ . A principle of material design for TSM based on quasi-1D crystals with nonsymmorphic crystal symmetry is provided also in this section. Finally discussions and a summary are presented in Sec. IV.

**II. CRYSTAL STRUCTURE**

The  $BaMX_3$  ( $M = V, Nb, \text{ or } Ta$ ;  $X = S \text{ or } Se$ ) is a group of quasi-one-dimensional crystals adopting hexagonal structure with the space group of  $P6_3/mmc$  (No. 194) [20,21] as shown in Fig. 1.  $M$  atoms are surrounded by octahedra of  $X$  atoms, and these octahedra form linear chains along the  $\hat{z}$  axis by sharing common surfaces. Those chains are lined up and arranged into a trigonal lattice in the  $x$ - $y$  plane with Ba atoms filling the space between the chains. As the interchain distance is much larger than the intrachain distance, these materials are considered to be quasi-one-dimensional crystals.

\*qfliang@usx.edu.cn

†hmweng@iphy.ac.cn

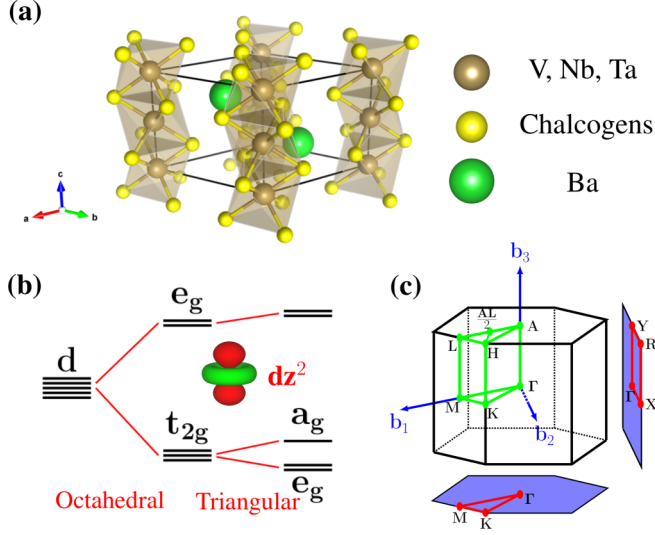


FIG. 1. (a) Unit cell of hexagonal  $BaMX_3$ . Large (green), medium (yellow), and small (brown) spheres denote the Ba, M, and X atoms. (b) Splitting of  $d$  orbitals under the crystal fields. The crystal field of an  $MX_3$  octahedron splits the fivefold  $d$  orbitals into twofold  $e_g$  and threefold  $t_{2g}$  orbitals. The crystalfield of the hexagonal lattice further splits the threefold  $t_{2g}$  orbitals into twofold  $e'_g$  and  $a_g$  orbitals.  $a_g$  has the character of the  $d_{3z^2-r^2}$  orbital shown in the inset. (c) The Brillouin zone of  $BaMX_3$ . Shaded planes are the projected 2D Brillouin zone to different crystal facets.

Each unit cell contains two formula units of  $BaMX_3$  and thus has two M atoms, labeled by A and B. Under the crystal field of the surrounding  $MX_3$  octahedra, the  $d$  orbitals of the two M atoms are split into twofold  $e_g$  orbitals and threefold  $t_{2g}$  orbitals. The threefold  $t_{2g}$  orbitals are further split into twofold  $e'_g$  orbitals and a single  $a_g$  orbital by the triangle crystal field of the ionic chain array [see Fig. 1(b) for this evolution of  $d$  orbitals]. The character of the wave function, mostly composed of the  $a_g$  manifold, is the  $d_{3z^2-r^2}$  atomic orbital, as shown in the inset of Fig. 1(b). With this quasi-1D crystal structure, the first-principles calculations of  $BaMX_3$ 's electronic structure were performed by using the Vienna *ab initio* simulation package (VASP) [22] with the generalized gradient approximation [23] in the projector augmented-wave method [24]. The Hubbard  $U$  is simulated through Dudarev's method [25] by setting  $(U - J)_V = 5.0$  eV and  $(U - J)_{Ta} = 2.0$  eV. Slightly changing the  $U - J$  value will not change the conclusion of this work. Tight-binding Hamiltonians are constructed based on the maximally localized Wannier functions (MLWFs) [26], and from these Hamiltonians surface band structures are calculated for slabs of  $BaMX_3$ .

### III. ELECTRONIC STRUCTURES

#### A. Node surface in $BaVS_3$

First, we investigate the electronic structure of  $BaVS_3$  in which the effect of SOC can be safely ignored. It is in a paramagnetic phase at room temperature. It is reported that  $BaVS_3$  undergoes a structure phase transition at 240 K and then enters into an insulating state through a metal-insulator phase transition at 70 K, with the nature of insulating state still being

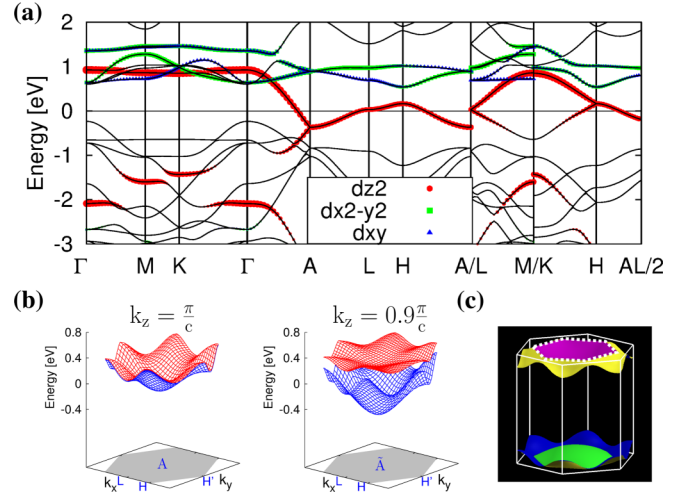


FIG. 2. Node surface in  $BaVS_3$  under room-temperature paramagnetic phase with negligible spin-orbit coupling. (a) Band dispersions of  $BaVS_3$ . The orbital natures are represented by circles (red), squares (green), and triangles (blue) for the  $d_{3z^2-r^2}$ ,  $d_{x^2-y^2}$ , and  $d_{xy}$  orbitals. (b) 3D plot of the bands in the  $k_z = \pi/c$  (left) and  $k_z = 0.9\pi/c$  (right) planes. (c) Fermi surface of  $BaVS_3$ . Dashed lines highlight the contact boundary between two partitions of the Fermi surface around  $k_z = \pi/c$ .

in debate. Here we are only interested in the high temperature paramagnetic state. The corresponding band structure is shown in Fig. 2(a). By analyzing the separated contributions from different  $d$  orbitals, we find the electronic states at the Fermi surface mainly consist of  $a_g$  orbitals. Notably, one can find that the conduction and valence bands exactly stick together along the high-symmetry paths  $A-L-H-A$ , while for another path,  $\Gamma-M-K-\Gamma-A$ , they are split [see Fig. 1(c) for the definitions of high-symmetry points]. The dispersions of these bands are small in the  $k_z = 0$  and  $k_z = \pi/c$  planes but large along the  $k_z$  direction, indicating the quasi-one-dimensional nature of  $BaVS_3$  crystal. By inspecting the band structure along a path off the high symmetry directions, namely  $H-AL/2$  with  $AL/2$  being the middle point of path  $A-L$ , one finds the degeneracy remains, and we may guess that the degeneracy takes place throughout the  $k_z = \pi/c$  plane. The conjecture is readily confirmed by the 3D plotting of band structure in Fig. 2(b). We fix the value of  $k_z$  at  $\pi/c$  but vary  $k_x$  and  $k_y$ . It is clearly seen that the conduction and valence bands are exactly overlapping at the  $k_z = \pi/c$  plane, which is the node surface with band touching points, or equivalently the Dirac nodal points, in it. Slightly deviating off this plane, i.e.,  $k_z = 0.9\pi/c$ , the degeneracy is split. The nodal points are not on the same energy level and the Fermi level cuts the node surface only at a continuous 1D line on the  $k_z = \pi/c$  plane, which connects the hole and electron pockets of the Fermi surface indicated with different colors in Fig. 2(c).

To the best of our knowledge, this is the first time that a node surface with conduction and valence band-touching nodes has been revealed in a realistic material. From a band-theory point of view, one would expect that the two  $a_g$  orbitals in a  $BaVS_3$  unit cell may form bonding and antibonding bands, and the two valence electrons provided by

the  $V^{+4}$  ions will fully occupy the bonding band and leave the antibonding one empty, making the material a band insulator. This naive band-theory picture, however, fails in the present case due to the nonsymmorphic crystal symmetry contained in the  $P6_3/mmc$  group [27]. The nonsymmorphic symmetry is a crystal symmetry which cannot be decomposed into the product of a lattice translation and a point-group operation. It has long been known [28] that nonsymmorphic symmetries make energy bands “stick together” at the boundary of the BZ. The node surface presented in our work therefore is a faithful demonstration of this physics as checked by the symmetry analysis below.

The symmetries participating to protect the degeneracy at the  $k_z = \pi/c$  plane are the time-reversal symmetry  $\mathcal{T} = \mathcal{K}$ , with  $\mathcal{K}$  being the complex conjugation (in the case without spin-orbit coupling), space inversion  $\mathcal{I}$ , and the skew axial symmetry  $\mathcal{S}_z = \{C_{2z} | \mathbf{T}_z = \mathbf{c}/2\}$ , a nonsymmorphic symmetry combining a half-vector translation along the  $\hat{c}$  axis and a twofold rotation about the  $\hat{z}$  axis. From these symmetries, two compound symmetries,  $\mathcal{C} = \mathcal{I}\mathcal{T}$  and  $\mathcal{S} = \mathcal{I}\mathcal{S}_z$ , are constructed.  $\mathcal{C}$  is preserved at any  $\mathbf{k}$  point of the BZ, while  $\mathcal{S}$  is respected at the  $k_z = 0$  and  $k_z = \pi/c$  planes. Applying  $\mathcal{S}$  twice on the lattice can bring the system back to its starting point; one has  $\mathcal{S}^2 = 1$ , and the corresponding eigenvalues of  $\mathcal{S}$  are  $\pm 1$ , which can be used to label the eigenstates of the Hamiltonian. Due to the anticommutation of  $\mathcal{C}$  and  $\mathcal{S}$  on the  $k_z = \pi/c$  plane (see Appendix A 1 for the derivation), the action of  $\mathcal{C}$  switches each eigenstate to its degenerate partner of opposite  $\mathcal{S}$  label, ensuring the twofold degeneracy of energy bands on the entire  $k_z = \pi/c$  plane, as found in Fig. 2(b). The details of the symmetry consideration and the derivation of the actions of the symmetry operators are summarized in Appendix A 1.

### B. Symmetry guaranteed nodal lines in BaTaS<sub>3</sub>

If SOC is included, the above discussion is not valid and the node surface of  $k_z = \pi/c$  plane will not persist. Luckily, for BaVS<sub>3</sub> the effective SOC splitting in the V's  $a_g$  bands is vanishingly small (about 1–2 meV), and thus the conduction and valence bands can still be considered degenerate at room temperature paramagnetic phase. However, for heavier  $M = \text{Nb}$  and  $\text{Ta}$ , the SOC is large and its effect has to be taken into account. In Fig. 3(a), we show the band structure of BaTaS<sub>3</sub> with SOC turned on. The inclusion of SOC lifts the degeneracy of bands at a general  $\mathbf{k}$  point in the the node surface  $k_z = \pi/c$  plane, as seen from the splitting of energy bands along  $L-H-A$  paths. Surprisingly, one can still find that, along a special path  $A-L$ , the energy bands remain fourfold degenerate (counting both spin and orbital degrees of freedom), forming a so-called node-line structure with Dirac nodes along it. In Fig. 3(b) we also plot a 3D band structure in  $k_z = \pi/c$ . Color gradients are used to indicate the energy splitting in the conduction and valence bands. In this plot and its contour projection onto the bottom  $k_z = \pi/c$ , three node lines related by  $C_{3z}$  rotation symmetry are found along the high-symmetry paths  $k_x = 0$  and  $k_x = \pm\sqrt{3}k_y$ .

The existence of nodelines also changes the Fermi surface around the  $k_z = \pi/c$  plane as shown in Fig. 3(c). Due to the nonzero band dispersion of the nodelines, the Fermi level cuts

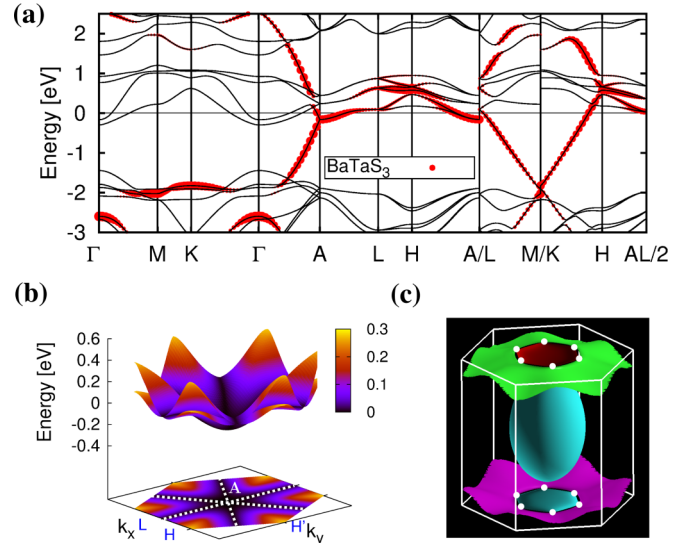


FIG. 3. Node lines in BaTaS<sub>3</sub> with strong spin-orbit coupling. (a) Band structure of BaTaS<sub>3</sub>. The orbital characteristic of the  $a_g$  band is highlighted by circles (red). (b) 2D plot of the bands in  $k_z = \pi/c$  plane. The gradually varied colors indicate the splitting of the bands. The darkest lines along  $A-L$  paths are node lines, denoted in the bottom contour plot by dashed lines. (c) Full view of the Fermi surface of BaTaS<sub>3</sub>. The contact points between the two partitions of the Fermi surface around  $k_z = \pi/c$  are highlighted by solid circles (white).

these lines at six discrete points. In the 3D Fermi surface plot, it is readily found that the Fermi lines connecting two different colors in the spinless case [Fig. 2(c)] now evolve into six separated contact points on the  $A-L$  paths. Comparing with the Fermi surface of BaVS<sub>3</sub> in Fig. 2(c), the additional ellipsoid-shaped Fermi surface surrounding the  $\Gamma$  point is from the two  $e'_g$  bands, as clearly shown in the band structure in Fig. 3(a).

Now let us discuss the symmetry protection of the fourfold degenerate node lines in the presence of SOC. The derivations of the actions of symmetry operators and their associated commutation relations are given in Appendix A 2. In the spinful case, the time-reversal operator is expressed as  $\mathcal{T} = i s_y \mathcal{K}$ , and thus  $\mathcal{T}^2 = -1$ . The skew axis  $\mathcal{S}_z$  now also acts on the spin space,  $\mathcal{S}_z : (s_x, s_y, s_z) \mapsto (-s_x, -s_y, s_z)$ . Applying it twice rotates the spin by  $2\pi$ , giving a minus sign for a spin-1/2 system. Since applying  $\mathcal{S} = \mathcal{I}\mathcal{S}_z$  twice on the real space brings the system back to its origin, one finds that the square of  $\mathcal{S}$  becomes  $\mathcal{S}^2 = -1$  at its invariant plane  $k_z = \pi/c$ . Notice that  $\mathcal{I}$  does not act on spin space. Then the eigenstates of Bloch Hamiltonian can be labeled by the eigenvalues  $\pm i$  of  $\mathcal{S}$ ,  $\mathcal{S}|\phi^\pm(\mathbf{k})\rangle = \pm i|\phi^\pm(\mathbf{k})\rangle$ . Unlike the spinless case, applying  $\mathcal{C}$  on  $|\phi^\pm(\mathbf{k})\rangle$  translates it to its Kramer partner with the same  $\mathcal{S}$  label. Thus, the two Kramer pairs with opposite  $\mathcal{S}$  label are not related and generally the bands should be twofold degenerate. Therefore, extra symmetries are needed to provide the protection of the node lines. We find that the mirror symmetry  $\mathbf{M}_x$  plays this role.  $\mathbf{M}_x$  acts both on the real space and spin space. It takes an anticommutation relation with  $\mathcal{S}$  on the intersection line of its invariant plane  $k_x = 0$  and the invariant plane of  $\mathcal{S}$ ,  $k_z = \pi/c$ . Because of  $\{\mathbf{M}_x, \mathcal{S}\} = 0$ ,



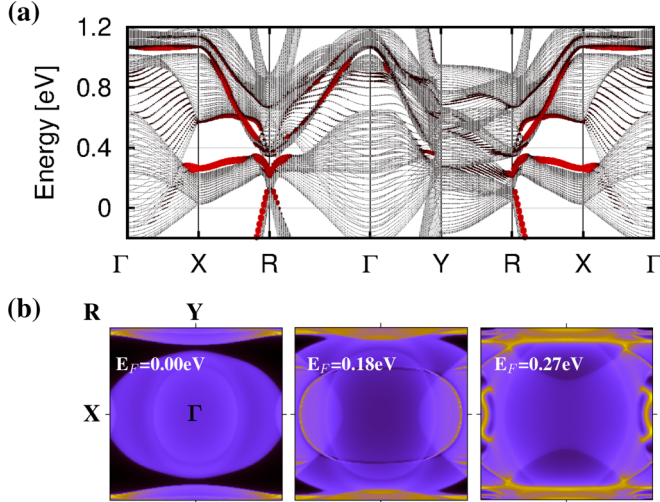


FIG. 4. Band structure of a 20-unit-cell-thick slab of BaTaS<sub>3</sub> with  $\{-110\}$  face. (a) Surface bands are highlighted by the thickness and color of the lines, scaled by the weight of surface contribution to the eigenstates. (b) Surface local density of states at different Fermi energies,  $E_F = 0.0$  eV (left), 0.18 eV (middle), and 0.27 eV (right).

applying  $\mathbf{M}_x$  on  $|\phi^\pm(\mathbf{k})\rangle$  will translate the state to a degenerate state with opposite  $S$  label. Therefore, with the help of  $\mathbf{M}_x$ , the two Kramer pairs of opposite  $S$  eigenvalues are now related by  $\mathbf{M}_x$  at the high-symmetry path  $k_x = 0$  on  $k_z = \pi/c$ , proving the existence of the fourfold degenerate node lines.

The node lines bring about surface states on the surface of BaTaS<sub>3</sub>, which is another demonstration of the nontrivial topology of the node line. In Fig. 4(a) we plot the surface electronic structure of a 20-unit-cell-thick BaTaS<sub>3</sub> slab with  $\{-110\}$  facet. From the figure, one can see segments of thick (red) lines inside the local “band gap” which are mainly contributed by the surface layers. When the surface bands immerse into bulk bands, the hybridization between the surface and the bulk bands will smear out the surface contribution. By using recursive Green’s function method, we calculated the surface Green’s function at the  $\{-110\}$  surface, and the obtained densities of states are plotted in Fig. 4(b) for Fermi energies  $E_F = 0.0$ , 0.18, and 0.27 eV. Bright lines highlighting the surface states’ contribution can be easily seen in these figures. On the other hand, drumhead-like flat surface bands observed in graphene networks [12] and Cu<sub>3</sub>PdN [14], however, are not found here due to the large dispersions of the node lines.

The observation of surface states at the slab’s surface is unexpected because the symmetries that protect the node lines are broken at the surfaces. This is understood from the nontrivial Berry phase  $\pi$  associated with each node line [7,16]. In order to verify this point, we construct an effective four-band Hamiltonian for BaTaS<sub>3</sub> in which the two  $a_g$  orbitals of Ta are considered (see in Appendix B for the construction of the Hamiltonian). The low-energy Hamiltonian around a point on the node-line  $\mathbf{k}_0 = (0, k_y, \pi/c)$  is written as

$$H_{\mathbf{q}} = \epsilon(\mathbf{k}) + q_z \tau_y s_x + q_z \tau_x + q_x \tau_y s_z, \quad (1)$$

with  $\mathbf{q} = (q_x, q_y, q_z)$  being a small deviation from  $\mathbf{k}_0$ .  $\tau$  denotes the orbital degree of freedom, and the dependency of  $H_{\mathbf{q}}$  on

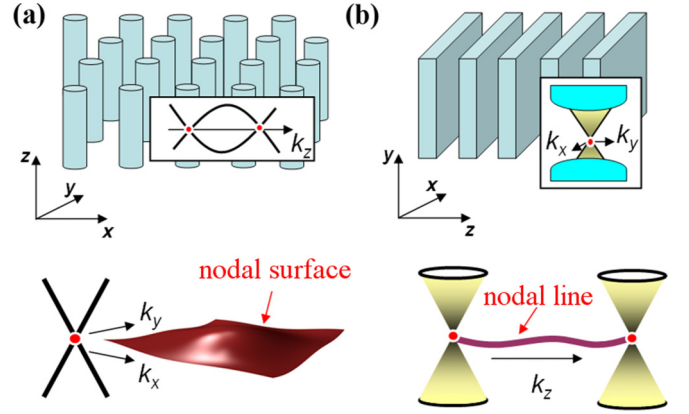


FIG. 5. Material design for TSMs. (a) (top) Parallel arrangement of 1D ionic chains. The inset shows the band structure of a single ionic chain which contains two crossing points at the boundary of the BZ,  $k_z = \pm\pi/c$ . (bottom) The twofold crossing point forms a 2D node-surface degeneracy when the chains are arranged into lattice in the  $x$ - $y$  plane. (b) (top) Stacking of TI layers to realize a topological semimetal. The inset shows the 2D Dirac cone band structure of the TI surface state. (bottom) The Dirac point forms a node line when the layers are stacked up in the  $z$  direction.

$q_y$  is contained in  $\epsilon(\mathbf{k})$  based on the symmetry consideration. As  $\epsilon(\mathbf{k})$  is not important for the solutions of (1), we omit it in the following discussion. The effective model (1) has a symmetry  $\tau_x s_z$  whose eigenvectors build up a unitary matrix that block-diagonalizes  $H_{\mathbf{q}}$ . By using an isospin-rotation and rescaling of  $q_z$ , one can finally rewrite the Hamiltonian in the nonzero subblock into the form

$$H_{\mathbf{q}} = \begin{bmatrix} 0 & \tilde{q}_z + i\tilde{q}_x \\ \tilde{q}_z - i\tilde{q}_x & 0 \end{bmatrix}.$$

When  $\tilde{\mathbf{q}}$  transverses along a closed loop circling the node line, the wave function of the occupied state accumulates a nonzero Berry phase  $\pi \pmod{2\pi}$ , demonstrating the nontrivial topology of the node line.

### C. Parallel ionic chains: Material design for mode-surface and node-line states

Our work provides a principle for material design: creating TSMs through arrangement of ionic chains in parallel. Previously, Balents *et al.* [19] and Phillips *et al.* [17] considered a layer-stacking approach to construct TSMs. In their scheme, the use of TI layers provides Dirac points from the TI layers’ surface states [see Fig. 5(b)]. When the TI layers are stacked along the  $\hat{z}$  axis, the Dirac points traverse along the  $k_z$  direction and form a node line in the 3D BZ. The node line will persist or be split into discrete Weyl points [19] depending on the details of the interlayer couplings and the magnetization of the magnetic layers [17].

Alternatively, here we propose to construct TSMs by parallel arrangement of ionic chains. The method is schematically shown in Fig. 5(a). In  $\text{BaMX}_3$ , the individual  $\text{MX}_3$  chain also respects the skew symmetry  $S_z$ , which guarantees an energy band crossing at the BZ’s boundary,  $k_z = \pm\pi/c$ . The parallel arrangement of the ionic chains then introduces interchain coupling. Due to the interchain coupling, the crossing point

translates along the  $k_x$  and  $k_y$  directions and builds up a 2D band touching at the 3D BZ's boundary [see the bottom of Fig. 5(b)]. The inclusion of hopping parameters along the  $x$ - $y$  plane usually breaks the degeneracy of the Dirac point at a general  $\mathbf{k}$  point where  $\mathcal{S}_z$  is broken. Luckily, for the present case this nonsymmorphic symmetry is respected at the whole  $k_z = \pi/c$  plane and the node-surface persists. When SOC is switched on, the node-surface degeneracy is lifted generally. However, mirror planes containing the  $\hat{z}$  axis are presented in the  $P6_3/mmc$  group. The node surface reduces into node lines at the high-symmetry paths where the mirror planes intersect with the node surface. This is a new route of realizing TSMs with peculiar symmetry-guaranteed node surface or node lines. It is worth noting that, with a similar strategy, Gibson *et al.* [29] have successfully designed Dirac semimetals in quasi-1D ionic crystals  $\text{TiMo}_3\text{Te}_3$  and  $\text{HfI}_3$  which contain a nonsymmorphic gliding plane or skew axis in their crystal symmetry groups.

#### IV. DISCUSSIONS AND CONCLUSIONS

We notice that the general physics of band-sticking in nonsymmorphic crystals has already been pointed out by Parameswaran *et al.* [27], and some first-principles calculations have been done on the family of  $\text{BaMX}_3$  [30–32]. However, the topological features of such 2D degeneracy of conduction and valence bands are revealed for the first time, to the best of our knowledge. The node lines induced by strong SOC from the node surface without SOC are quite different from those proposed previously [12–15], in which the node lines are only stable in the absence of SOC. Some proposals claim the stability of node lines with the inclusion of SOC, such as those in  $\text{SrIrO}_3$  [10] and  $\text{PbTaSe}_2$  [16]. These node lines are off the high-symmetry paths and originate from accidental band touching, and there is no guarantee of their existence. However, the node lines in the present case are fourfold degenerate and are guaranteed to happen at the high-symmetry paths.

We also notice that, by decreasing the temperature,  $\text{BaVS}_3$  experiences first a structure phase transition from the room temperature hexagonal phase to the low temperature orthorhombic phase, and then a paramagnetic-to-antiferromagnetic phase transition under which the material becomes a gapped state. In  $\text{BaTaS}_3$  and  $\text{BaTaSe}_3$  [33,34], semiconductor-metal transitions are observed at low temperature; however, no clear signature of structure or magnetic transition is detected, and the nature of the semiconductor-metal transition is still under debate. Whether this phase transition is topological in nature [27] or not, and what is the relation between the observed phase transitions and the node surface and node lines discovered in the present work, need further investigations.

In summary, we have found a 2D node surface at the  $k_z = \pi/c$  plane in the band structure of  $\text{BaVS}_3$  with negligible SOC (about 1–2 meV). Such a novel TSM is protected by the nonsymmorphic symmetry  $\mathcal{S}_z$ . In its family compound  $\text{BaTaS}_3$  with strong SOC, the node surface evolves into node lines along three high symmetry paths on the  $k_z = \pi/c$  plane. The symmetries that protect the node lines are the nonsymmorphic skew axial symmetry  $\mathcal{S}_z$ , mirror symmetry  $\mathbf{M}_x$ , inversion symmetry  $\mathcal{I}$ , and time-reversal symmetry  $\mathcal{T}$ . Two-orbital effective models are constructed to compute the

nontrivial Berry phase associated with each node line. The physics of the node lines originating from the nonsymmorphic symmetry is analyzed. Surface states are observed in a slab of  $\text{BaTaS}_3$  despite the large dispersions of node lines and the breaking of crystal symmetries at the surface. Our work paves a way to design materials with peculiar energy band degeneracy through arrangement of ionic chains in parallel.

#### ACKNOWLEDGMENTS

The work is supported by the National Natural Science Foundation of China (NSFC) (Grants No.11574215, No. 11274359, and No. 11422428). Q.F.L. acknowledges support from the Scientific Research Foundation for Returned Overseas Chinese Scholars, State Education Ministry of China. H.M.W. is supported by the National 973 program of China (Grants No. 2011CBA00108 and No. 2013CB921700), and the “Strategic Priority Research Program (B)” of the Chinese Academy of Sciences (Grant No. XDB07020100).

#### APPENDIX A: SYMMETRY ANALYSIS

##### 1. The spinless case

Let us prove that in a crystal preserving the time-reversal symmetry  $\mathcal{T}$ , inversion symmetry  $\mathcal{I}$ , and a two-fold skew axis along  $\hat{z}$ ,  $\mathcal{S}_z : (x, y, z, t) \mapsto (-x, -y, z + \frac{1}{2}, t)$ , the energy bands at the  $k_z = \pi/c$  plane will be twofold degenerated if the spin effect is excluded. By using these three symmetries, one can compose two compound symmetries,  $\mathcal{C} = \mathcal{IT}$  and  $\mathcal{S} = \mathcal{IS}_z$ . In the real space,  $\mathcal{C}$  and  $\mathcal{S}$  act as

$$\begin{aligned}\mathcal{C} : (x, y, z, t) &\mapsto (-x, -y, -z, -t), \\ \mathcal{S} : (x, y, z, t) &\mapsto (x, y, -z - \frac{1}{2}, t).\end{aligned}\tag{A1}$$

In momentum space, one easily finds that all the  $\mathbf{k}$  points are invariant points under the action of  $\mathcal{C}$ . On the other hand,  $\mathcal{S}$  translates  $(k_x, k_y, k_z)$  to  $(k_x, k_y, -k_z)$ , which means  $k_z = 0$  and  $k_z = \pi/c$  are the two invariant planes of  $\mathcal{S}$ . Applying  $\mathcal{S}$  twice, the coordinates in the real space return back and one finds  $\mathcal{S}^2 = 1$ , which means the eigenvalues of  $\mathcal{S}$  are  $\pm 1$  and one can use them to label the Bloch states  $|\psi(\mathbf{k})\rangle$  of the system's Hamiltonian by  $\mathcal{S}|\psi^\pm(\mathbf{k})\rangle = \pm|\psi^\pm(\mathbf{k})\rangle$ .

We find that, under the action of  $\mathcal{C}$ , each eigenstate  $|\psi^\pm(\mathbf{k})\rangle$  is switched to a degenerate state of an opposite  $\mathcal{S}$  label. Before showing this, we first prove that  $\mathcal{C}$  and  $\mathcal{S}$  take an anticommutation relation at  $k_z = \pi/c$ . By using Eq. (A1), one obtains

$$\begin{aligned}\mathcal{SC} : (x, y, z, t) &\mapsto (-x, -y, z - \frac{1}{2}, -t), \\ \mathcal{CS} : (x, y, z, t) &\mapsto (-x, -y, z + \frac{1}{2}, -t),\end{aligned}\tag{A2}$$

from which one finds in  $\mathbf{k}$ -space

$$\mathcal{CS} = \mathbf{T}_c \mathcal{SC} = e^{ik_z c} \mathcal{SC},\tag{A3}$$

with  $\mathbf{T}_c$  being the translation along the  $\hat{z}$  axis by one primary vector  $\mathbf{c}$ . Therefore the anti-commutator of  $\mathcal{C}$  and  $\mathcal{S}$  becomes zero,  $\{\mathcal{C}, \mathcal{S}\} = 0$ , at  $k_z = \pi/c$ . With this anticommutation relation, one can prove that  $\mathcal{C}$  relates the eigenstates to their degenerate partners of opposite  $\mathcal{S}$  label as follows:

$$\mathcal{SC}|\psi^\pm(\mathbf{k})\rangle = e^{-i\frac{\pi}{c}c} \mathcal{CS}|\psi^\pm(\mathbf{k})\rangle = \mp \mathcal{C}|\psi^\pm(\mathbf{k})\rangle.\tag{A4}$$

Then, on the  $k_z = \pi/c$  plane, one proves that each band is twofold degenerate. We should stress here that, for the case of no spin, actually the inversion  $\mathcal{I}$  is not necessary for the degeneracy at  $k_z = \pi/c$ . We can use an alternative compound symmetry  $\Theta = \mathcal{T}\mathcal{S}_z$  to protect the degeneracy. It is easy to check that it takes  $\Theta^2 = -1$  at the  $k_z = \pi/c$  plane, which ensures a Krammer degeneracy with the two related states labeled by eigenvalues  $\pm i$  of  $\Theta$ . However, in the following spinful case,  $\Theta$  is not enough to protect the node lines. For the purpose of consistency with the spinful case below, we use the same compound symmetries  $\mathcal{I}\mathcal{S}_z$  and  $\mathcal{I}\mathcal{T}$  in the spinless case.

## 2. The effect of spin-orbit coupling

Including the spin degree of freedom and the effect of SOC generally splits the fourfold degeneracy (counting both spin and orbit degree of freedom) at  $k_z = \pi/c$ . In this spinful case,  $\mathcal{S}_z$  also acts on the spin space,  $\mathcal{S}_z : (s_x, s_y, s_z) \mapsto (-s_x, -s_y, s_z)$ . The square of  $\mathcal{S}_z$  then rotates the spins by  $2\pi$ , contributing a minus sign for the spin- $\frac{1}{2}$  system. Therefore the square of  $\mathcal{S} = \mathcal{I}\mathcal{S}_z$  becomes  $\mathcal{S}^2 = -1$ , and  $\mathcal{S}$  now has eigenvalues  $\pm i$ , which again can be used to label the eigenstates of the Bloch Hamiltonian,  $\mathcal{S}|\phi^\pm(\mathbf{k})\rangle = \pm i|\phi^\pm(\mathbf{k})\rangle$ . Unlike the spinless case, the action of  $\mathcal{C} = \mathcal{I}\mathcal{T}$  on the eigenstate  $|\phi^\pm(\mathbf{k})\rangle$  only switches it to a partner state of the same  $\mathcal{S}$ -label, even though the anticommutation relation of  $\mathcal{C}$  and  $\mathcal{S}$  is retained. This point is easily checked as

$$\begin{aligned} \mathcal{S}\mathcal{C}|\phi^\pm(\mathbf{k})\rangle &= e^{-ik_z c} \mathcal{C}\mathcal{S}|\phi^\pm(\mathbf{k})\rangle \\ &= -\mathcal{C}(\pm i|\phi^\pm(\mathbf{k})\rangle) \\ &= \pm i\mathcal{C}|\phi^\pm(\mathbf{k})\rangle. \end{aligned} \quad (\text{A5})$$

Equation (A4) is used in the first line of Eq. (A5), and the last equality in Eq. (A5) is obtained based on the fact that the time-reversal operator  $\mathcal{T} = is_y\mathcal{K}$  contained in  $\mathcal{C}$  conjugates  $i$  to  $-i$ .

As  $\mathcal{C}$  only related the eigenstate to its partner with the same  $\mathcal{S}$  label, we only obtain two Krammers pairs that cannot be related by symmetry  $\mathcal{S}$  and  $\mathcal{C}$  only. To explain the fourfold degenerate node lines of BaTaS<sub>3</sub>, we need other symmetries. We find it is the mirror symmetry  $\mathbf{M}_x : (x, y, z) \mapsto (-x, y, z)$  that provides the needed protection for these node lines. The implication is that the high symmetry path  $k_x = 0$  at  $k_z = \pi/c$  is just the intersecting line of the invariant plane  $k_x = 0$  of  $\mathbf{M}_x$  and the invariant plane  $k_z = \pi/c$  of  $\mathcal{S}$ . On this invariant line, action of  $\mathbf{M}_x$  will transform the eigenstate  $|\phi^\pm(\mathbf{k})\rangle$  to a partner of an opposite  $\mathcal{S}$  label, which then relates the two Krammer pairs and ensures a fourfold degenerate node line. Before clarifying this point, we first prove that  $\mathbf{M}_x$  anticommutes with  $\mathcal{S}$ . It is easily checked that, in the real space, action of  $\mathbf{M}_x$  and  $\mathbf{M}_x\mathcal{S}$  on the coordinate leads to the same result. The anticommutation relation of  $\mathbf{M}_x$  and  $\mathcal{S}$  comes from their action on the spin space. In spin space,  $\mathcal{S}$  reflects  $s_x$  and  $s_y$  but keeps  $s_z$  invariant, from which one can express its action by  $\exp(i\pi/2\hat{s}_z) = i\hat{s}_z$ . Similarly, the action of  $\mathbf{M}_x$  on the spin is expressed by  $\exp(i\pi/2\hat{s}_x) = i\hat{s}_x$ . It is the action of  $\mathbf{M}_x$  and  $\mathcal{S}$  on the spin space that ensures the anticommutation relation,  $\{\mathcal{S}, \mathbf{M}_x\} = 0$ . By applying  $\mathbf{M}_x$  on the eigenstate  $|\phi^\pm(\mathbf{k})\rangle$ , one

then finds

$$\begin{aligned} \mathbf{M}_x|\phi^\pm(\mathbf{k})\rangle &= -\mathbf{M}_x\mathcal{S}|\phi^\pm(\mathbf{k})\rangle \\ &= -\mathbf{M}_x(\pm i|\phi^\pm(\mathbf{k})\rangle) \\ &= \mp i\mathbf{M}_x|\phi^\pm(\mathbf{k})\rangle. \end{aligned} \quad (\text{A6})$$

Equations (A5) and (A6) finally finish the proof that at  $k_x = 0$  on the  $k_z = \pi/c$  plane there must be a four fold degenerate node line guaranteed by symmetries  $\mathcal{S} = \mathcal{I}\mathcal{S}_z$ ,  $\mathcal{C} = \mathcal{I}\mathcal{T}$ , and  $\mathbf{M}_x$ . The node lines at  $k_x = \pm\sqrt{3}k_y$  on  $k_z = \pi/c$  then result from the  $C_{3z}$  rotation.

## APPENDIX B: EFFECTIVE HAMILTONIAN

There are two active  $d_{3z^2-r^2}$  orbitals hosted on Ta atom in the unit cell, and they compose the electronic states around the Fermi surface. When SOC is turned off, we can use these two orbitals, denoted by  $A$  and  $B$ , to construct a  $2 \times 2$  Hamiltonian at each  $\mathbf{k}$  point in the momentum space:

$$\hat{H}_0(\mathbf{k}) = \begin{bmatrix} H_{AA}(\mathbf{k}) & H_{AB}(\mathbf{k}) \\ H_{AB}^*(\mathbf{k}) & H_{BB}(\mathbf{k}) \end{bmatrix}. \quad (\text{B1})$$

Here  $|\eta, \mathbf{k}\rangle = \frac{1}{\sqrt{N}} \sum_n e^{i\mathbf{k}\cdot\mathbf{r}_{n\eta}} \psi(\mathbf{r} - \mathbf{r}_{n\eta})$  are the two basis functions, with  $\eta = A, B$  denoting the orbitals.  $\psi(\mathbf{r} - \mathbf{r}_{n\eta})$  is the local  $d_{3z^2-r^2}$  wave function centered on atom site  $\mathbf{r}_{n\eta}$  in the  $n$ th unit cell. For the spinful Hamiltonian, We need to take the spin degree of freedom into consideration, and thus we define four basis functions  $|\eta, \mathbf{k}, \sigma\rangle$ , with  $\sigma = \uparrow$  or  $\downarrow$  denoting the spin direction. The Hamiltonian is then enlarged to a  $4 \times 4$  size,

$$H(\mathbf{k}) = \begin{bmatrix} H_{AA}^{\uparrow\uparrow}(\mathbf{k}) & H_{AB}^{\uparrow\uparrow}(\mathbf{k}) & H_{A\downarrow}^{\uparrow\downarrow}(\mathbf{k}) & H_{AB}^{\uparrow\downarrow}(\mathbf{k}) \\ & H_{BB}^{\uparrow\uparrow}(\mathbf{k}) & H_{BA}^{\uparrow\downarrow}(\mathbf{k}) & H_{BB}^{\uparrow\downarrow}(\mathbf{k}) \\ & & H_{AA}^{\downarrow\downarrow}(\mathbf{k}) & H_{AB}^{\downarrow\downarrow}(\mathbf{k}) \\ \dagger & & & H_{BB}^{\downarrow\downarrow}(\mathbf{k}) \end{bmatrix}. \quad (\text{B2})$$

The time-reversal operator  $\mathcal{T}$  now becomes  $\mathcal{T} = i\hat{s}_y\mathcal{K}$ , with  $\hat{s}_y = \begin{bmatrix} 0 & i \\ -i & 0 \end{bmatrix}$  being the Pauli matrix acting on the spin space. It reads

$$\begin{aligned} \mathcal{T}|\eta, \mathbf{k}, \sigma\rangle &= \text{sgn}(\sigma)|\eta, -\mathbf{k}, \bar{\sigma}\rangle, \\ \mathcal{T}H(\mathbf{k}) &= H(-\mathbf{k})\mathcal{T}, \end{aligned} \quad (\text{B3})$$

with the sign function  $\text{sgn}(\sigma)$  being  $= +1$  ( $-1$ ) for spin  $\uparrow$  ( $\downarrow$ ) and  $H(\mathbf{k}) = e^{-i\mathbf{k}\cdot\mathbf{r}}H(\mathbf{r})e^{i\mathbf{k}\cdot\mathbf{r}}$ . For the entries of Hamiltonian (B2), one finds

$$\begin{aligned} H_{\eta_1\eta_2}^{\sigma_1\sigma_2}(\mathbf{k}) &= \langle \eta_1, \mathbf{k}, \sigma_1 | H(\mathbf{k}) | \eta_2, \mathbf{k}, \sigma_2 \rangle \\ &= -\text{sgn}(\sigma_2) \langle \eta_1, \mathbf{k}, \sigma_1 | H(\mathbf{k}) \mathcal{T} | \eta_2, -\mathbf{k}, \bar{\sigma}_2 \rangle \\ &= -\text{sgn}(\sigma_2) \langle \eta_1, \mathbf{k}, \sigma_1 | \mathcal{T} [H(-\mathbf{k}) | \eta_2, -\mathbf{k}, \bar{\sigma}_2] \rangle \\ &= \text{sgn}(\sigma_2) \text{sgn}(\sigma_1) \langle \mathcal{T}(\eta_1, -\mathbf{k}, \bar{\sigma}_1) | \mathcal{T} \\ &\quad \times [H(-\mathbf{k}) | \eta_2, -\mathbf{k}, \bar{\sigma}_2] \rangle \\ &= \text{sgn}(\sigma_1) \text{sgn}(\sigma_2) [\langle \eta_2, -\mathbf{k}, \bar{\sigma}_2 | H(-\mathbf{k}) | \eta_1, -\mathbf{k}, \bar{\sigma}_1 \rangle] \\ &= \text{sgn}(\sigma_1) \text{sgn}(\sigma_2) H_{\eta_2\eta_1}^{\bar{\sigma}_2\bar{\sigma}_1}(-\mathbf{k}). \end{aligned} \quad (\text{B4})$$

To obtain the second and forth lines of the above equation, we use the transformation (B3) of the wave function for the right and left kets, respectively. The transformation of the Hamiltonian under  $\mathcal{T}$  is used to obtain the third line. To get the fifth line, we use the property of time-reversal symmetry  $\langle \mathcal{T}\phi | \mathcal{T}|\psi \rangle = \langle \psi | \phi \rangle$ .

The  $P6_3/mmc$  group also contains an inversion symmetry  $\mathcal{I} : (x, y, z) \mapsto (-x, -y, -z)$ .  $\mathcal{I}$  does not flip the spin and orbit indices, and the wave functions and Hamiltonian are transformed as

$$\begin{aligned} \mathcal{I}|\eta, \mathbf{k}, \sigma\rangle &= |\eta, -\mathbf{k}, \sigma\rangle, \\ \mathcal{I}H(\mathbf{k}) &= H(-\mathbf{k})\mathcal{I}. \end{aligned} \quad (\text{B5})$$

Applying Eq. (B5), one finds the consequence of applying  $\mathcal{I}$  onto the elements of Hamiltonian (B2):

$$H_{\eta_1\eta_2}^{\sigma_1\sigma_2}(k_x, k_y, k_z) = H_{\eta_1\eta_2}^{\sigma_1\sigma_2}(-k_x, -k_y, -k_z). \quad (\text{B6})$$

Applying Eqs. (B4) and (B6) successively one obtains

$$H_{\eta_1\eta_2}^{\sigma_1\sigma_2}(k_x, k_y, k_z) = \text{sgn}(\sigma_1) \text{sgn}(\sigma_2) H_{\eta_2\eta_1}^{\bar{\sigma}_2\bar{\sigma}_1}(k_x, k_y, k_z), \quad (\text{B7})$$

which reduces the Hamiltonian (B2) to the form

$$H(\mathbf{k}) = \begin{bmatrix} a(\mathbf{k}) & f(\mathbf{k}) & 0 & g(\mathbf{k}) \\ & b(\mathbf{k}) & -g(\mathbf{k}) & 0 \\ & & a(\mathbf{k}) & f^*(\mathbf{k}) \\ \dagger & & & b(\mathbf{k}) \end{bmatrix}, \quad (\text{B8})$$

where  $a(\mathbf{k})$  and  $b(\mathbf{k})$  are real functions, and  $f(\mathbf{k})$  and  $g(\mathbf{k})$  are complex functions.

Hamiltonian (B8) is mathematically equivalent to a linear combination of five Dirac matrices  $\Gamma_a$  together with the unit matrix  $\Gamma_0$ . The eigenvalues of Hamiltonian (B8) become fourfold degenerate only if the five coefficients of the Dirac matrices become zero; that is,  $a(\mathbf{k}) - b(\mathbf{k}) = f(\mathbf{k}) = g(\mathbf{k}) = 0$ , which, however, does not hold at a general  $\mathbf{k}$  point. Below we prove that this fourfold degenerate condition is readily fulfilled at three high-symmetry paths:  $k_x = 0$  and  $k_x = \pm\sqrt{3}k_y$  on the  $k_z = \pi/c$  plane, with the help of  $\mathcal{S}_z$  and a mirror symmetry  $\mathbf{M}_x : (x, y, z) \mapsto (-x, y, z)$ .

In real space, the skew axial symmetry  $\mathcal{S}_z$  flips the orbit indices. While in spin space, it keeps the  $s_z$  component invariant but reverse  $s_x$  and  $s_y$ , indicating that its action can be represented by  $i\hat{s}_z$ . Therefore the wave function and Hamiltonian transform as

$$\begin{aligned} \mathcal{S}_z|\eta, \mathbf{k}, \sigma\rangle &= ie^{-i\frac{k_z c}{2}} \text{sgn}(\sigma) |\bar{\eta}, -k_x, -k_y, k_z, \sigma\rangle, \\ \mathcal{S}_z H(\mathbf{k}) &= H(-k_x, -k_y, k_z) \mathcal{S}_z. \end{aligned} \quad (\text{B9})$$

With Eq. (B9), one finds the following relation for Bloch Hamiltonian (B8):

$$\begin{aligned} H_{\eta_1\eta_2}^{\sigma_1\sigma_2}(\mathbf{k}) &= \langle \eta_1, \mathbf{k}, \sigma_1 | H(\mathbf{k}) | \eta_2, \mathbf{k}, \sigma_2 \rangle \\ &= \langle \eta_1, \mathbf{k}, \sigma_1 | \hat{\mathcal{S}}_z^{-1} \hat{\mathcal{S}}_z H(\mathbf{k}) \hat{\mathcal{S}}_z^{-1} \mathcal{S}_z | \eta_2, \mathbf{k}, \sigma_2 \rangle \\ &= \langle \eta_1, \mathbf{k}, \sigma_1 | \hat{\mathcal{S}}_z^{-1} H(\tilde{\mathbf{k}}) \hat{\mathcal{S}}_z | \eta_2, \mathbf{k}, \sigma_2 \rangle \\ &= \langle \bar{\eta}_1, \tilde{\mathbf{k}}, \sigma_1 | H(\tilde{\mathbf{k}}) | \bar{\eta}_2, \tilde{\mathbf{k}}, \sigma_2 \rangle \\ &= \text{sgn}(\sigma_1) \text{sgn}(\sigma_2) H_{\bar{\eta}_1\bar{\eta}_2}^{\sigma_1\sigma_2}(-k_x, -k_y, k_z), \end{aligned} \quad (\text{B10})$$

with  $\tilde{\mathbf{k}} = (-k_x, -k_y, k_z)$ . Then a constraint for the spinful Hamiltonian (B8) is obtained:

$$H_{\eta_1\eta_2}^{\sigma_1\sigma_2}(k_x, k_y, k_z) = \text{sgn}(\sigma_1) \text{sgn}(\sigma_2) H_{\bar{\eta}_1\bar{\eta}_2}^{\sigma_1\sigma_2}(-k_x, -k_y, k_z). \quad (\text{B11})$$

Combining Eqs. (B6) and (B11), one arrives at the following important relation of Hamiltonian posed by symmetry  $\mathcal{S} = \mathcal{I}\mathcal{S}_z$ :

$$H_{\eta_1\eta_2}^{\sigma_1\sigma_2}(k_x, k_y, k_z) = \text{sgn}(\sigma_1) \text{sgn}(\sigma_2) H_{\bar{\eta}_1\bar{\eta}_2}^{\sigma_1\sigma_2}(k_x, k_y, -k_z). \quad (\text{B12})$$

Applying the transformation  $H_{\eta_1\eta_2}^{\sigma_1\sigma_2}(\mathbf{k} + \mathbf{G}) = e^{i\mathbf{G} \cdot \mathbf{r}_{\eta_1\eta_2}} H_{\eta_1\eta_2}^{\sigma_1\sigma_2}(\mathbf{k})$  to Eq. (B12) for  $k_z = \pi/c$ , one finds

$$\begin{aligned} H_{AB}^{\sigma_1\sigma_2}(k_x, k_y, \pi/c) &= \text{sgn}(\sigma_1) \text{sgn}(\sigma_2) H_{BA}^{\sigma_1\sigma_2}(k_x, k_y, -\pi/c) \\ &= \text{sgn}(\sigma_1) \text{sgn}(\sigma_2) e^{i\frac{2\pi}{c} \cdot \frac{c}{2}} H_{BA}^{\sigma_1\sigma_2}(k_x, k_y, \pi/c), \end{aligned} \quad (\text{B13})$$

so that

$$\begin{aligned} H_{AB}^{\uparrow\downarrow}(k_x, k_y, \pi/c) &= H_{BA}^{\uparrow\downarrow}(k_x, k_y, \pi/c), \\ H_{AB}^{\uparrow\uparrow}(k_x, k_y, \pi/c) &= -H_{BA}^{\uparrow\uparrow}(k_x, k_y, \pi/c), \end{aligned} \quad (\text{B14})$$

proving in Hamiltonian (B8) that

$$g(k_x, k_y, \pi/c) = 0, \quad \text{Re}[f(k_x, k_y, \pi/c)] = 0. \quad (\text{B15})$$

Applying Eq. (B12) to  $H_{AA}^{\uparrow\uparrow}(\mathbf{k})$ , one similarly obtains

$$H_{AA}^{\uparrow\uparrow}(k_x, k_y, \pi/c) = H_{BB}^{\uparrow\uparrow}(k_x, k_y, \pi/c), \quad (\text{B16})$$

which proves

$$a(k_x, k_y, \pi/c) = b(k_x, k_y, \pi/c). \quad (\text{B17})$$

Therefore, in the presence of  $\mathcal{I}$ ,  $\mathcal{T}$ , and  $\mathcal{S}_z$ , most elements of Hamiltonian (B8) vanish at the  $k_z = \pi/c$  plane, except for the imaginary part of  $H_{AB}^{\uparrow\downarrow}(k_x, k_y, \pi/c)$  and a diagonal element  $\epsilon(\mathbf{k}) = [a(k_x, k_y, \pi/c) + b(k_x, k_y, \pi/c)]/2$ .

It is possible to prove that  $\text{Im}[f(0, k_y, \pi/c)] = 0$  at the high-symmetry path  $k_x = 0$  on the  $k_z = \pi/c$  plane. To do so, we need an extra symmetry, which in the present case is a mirror symmetry  $\mathbf{M}_x$  with the mirror plane lying in the  $y$ - $z$  plane. In real space the mirror symmetry  $\mathbf{M}_x$  keeps the orbit indices invariant and inverts the  $x$  component of coordinates. In spin space, it keeps the spin component  $s_x$  invariant but reverses  $s_y$  and  $s_z$ , indicating its action on the spin space represented by  $i\hat{s}_x$ . Therefore the wave function and Hamiltonian transform as

$$\begin{aligned} \mathbf{M}_x|\eta, \mathbf{k}, \sigma\rangle &= i|\eta, -k_x, k_y, k_z, \bar{\sigma}\rangle, \\ \mathbf{M}_x H(\mathbf{k}) &= H(-k_x, k_y, k_z) \mathbf{M}_x. \end{aligned} \quad (\text{B18})$$

which indicates

$$H_{\eta_1\eta_2}^{\sigma_1\sigma_2}(k_x, k_y, k_z) = H_{\eta_1\eta_2}^{\bar{\sigma}_1\bar{\sigma}_2}(-k_x, k_y, k_z). \quad (\text{B19})$$

With Eq. (B19), one gets  $H_{AB}^{\uparrow\uparrow}(0, k_y, k_z) = H_{AB}^{\downarrow\downarrow}(0, k_y, k_z)$  and  $H_{AB}^{\uparrow\downarrow}(0, k_y, k_z) = H_{AB}^{\downarrow\uparrow}(0, k_y, k_z)$ , which proves

$$\text{Im}[f(0, k_y, k_z)] = 0, \quad \text{Re}[g(0, k_y, k_z)] = 0. \quad (\text{B20})$$



Summarizing the above discussion, we prove that there exists a node line at the  $k_x = 0$  path on the  $k_z = \pi/c$  plane for  $\text{BaMnX}_3$  when SOC is turned on. For the other two node lines at  $k_x = \pm\sqrt{3}k_y$  [see Fig. 3(b)], they can be produced by using the  $\hat{C}_3$  symmetry of the system, which rotates the  $k_x = 0$  node line to the  $k_x = \pm\sqrt{3}k_y$  directions.

We then expand the Hamiltonian around a point on the node line  $\mathbf{k} = (0, k_y, \pi/c) + (q_x, q_y, q_z)$ , with  $(q_x, q_y, q_z)$  being small deviations from the expanding point  $\mathbf{k}_0 = (0, k_y, \pi/c)$ . From the above Eqs. (B15), (B17), and (B20) one finds

$$\begin{aligned} \left. \frac{\partial g}{\partial q_x} \right|_{\mathbf{k}_0} &= 0, \quad \left. \frac{\partial g}{\partial q_y} \right|_{\mathbf{k}_0} = 0, \quad \text{Re} \left. \frac{\partial g}{\partial q_z} \right|_{\mathbf{k}_0} = 0, \\ \text{Re} \left. \frac{\partial f}{\partial q_x} \right|_{\mathbf{k}_0} &= 0, \quad \left. \frac{\partial f}{\partial q_y} \right|_{\mathbf{k}_0} = 0, \quad \text{Im} \left. \frac{\partial f}{\partial q_z} \right|_{\mathbf{k}_0} = 0, \\ \left. \frac{\partial a}{\partial q_i} \right|_{\mathbf{k}_0} &= \left. \frac{\partial b}{\partial q_i} \right|_{\mathbf{k}_0} \quad (i = x, y, z). \end{aligned} \quad (\text{B21})$$

from which the low energy Hamiltonian is obtained:

$$H_q = \epsilon(\mathbf{k}) + \alpha q_z \tau_y s_x + q_z \tau_x + q_x \tau_y s_z. \quad (\text{B22})$$

As  $\epsilon(\mathbf{k})$  is not important for the solution of Hamiltonian (B21), we omit it in the following discussions. The Hamiltonian (B22) takes a symmetry  $\tau_x s_y$ , and by using the unitary matrix  $U$  which diagonalizes  $\tau_x s_y$ ,

$$U = \frac{1}{\sqrt{2}} \begin{bmatrix} 1 & 0 & 1 & 0 \\ 0 & 1 & 0 & 1 \\ 0 & -i & 0 & i \\ -i & 0 & i & 0 \end{bmatrix}, \quad (\text{B23})$$

one can transform the Hamiltonian  $H_q$  into a block-diagonalized matrix  $\tilde{H}_q$ ,

$$\begin{aligned} \tilde{H}_q &= \epsilon(\mathbf{k}) + \frac{1}{\sqrt{2}} \\ &\times \begin{bmatrix} \alpha q_z & q_z + i q_x & 0 & 0 \\ q_z - i q_x & -\alpha q_z & 0 & 0 \\ 0 & 0 & -\alpha q_z & q_z + i q_x \\ 0 & 0 & q_z - i q_x & \alpha q_z \end{bmatrix}. \end{aligned} \quad (\text{B24})$$

For each nonzero subblock of Hamiltonian (B24), the diagonal terms are further moved to the off-diagonal entries through an isospin-rotation about the  $\tilde{\tau}_y$  axis  $\exp(i\pi/8\tilde{\tau}_y)$ . After a rescale of  $q_z$  by  $1/(\alpha^2 + 1)$ , one obtains a simple form of  $2 \times 2$  Hamiltonian,

$$H_{\tilde{q}} = \begin{bmatrix} 0 & \tilde{q}_z + i\tilde{q}_x \\ \tilde{q}_z - i\tilde{q}_x & 0 \end{bmatrix},$$

for each subblock. The occupied state has an eigenvalue of  $-\sqrt{\tilde{q}_x^2 + \tilde{q}_z^2}$ , with the corresponding eigen-vector being

$$\sqrt{2}/2 \begin{bmatrix} 1 \\ -\exp(-i\theta) \end{bmatrix}.$$

When  $\tilde{\mathbf{q}}$  traverses a closed loop circling the node line, the accumulated Berry phase is computed to  $\pi$  as follows:

$$\begin{aligned} \Phi_B &= -i \lim_{N \rightarrow \infty} \sum_{j=0}^{N-1} \log \langle j | j+1 \rangle \\ &= -i \lim_{N \rightarrow \infty} \sum_{j=0}^{N-1} \log \left( \frac{1 + \exp[i(\theta_{j+1} - \theta_j)]}{2} \right) \\ &= -i \int_0^{2\pi} \frac{id\theta}{2} = \pi, \end{aligned} \quad (\text{B25})$$

where the loop is discretized into  $N$  successive points labeled by  $j$  ( $j = 0, 1, 2, \dots, N-1$ ) with  $N = 0$ . The Berry phase  $\Phi_B$  here is only meaningful for modulo  $2\pi$ , as  $|N\rangle = e^{i2m\pi}|0\rangle$  is also well defined for condition  $N = 0$ , which will increase  $\Phi_B$  by  $2m\pi$ .

### APPENDIX C: TIGHT-BINDING MODEL

In this section we construct a tight-binding (TB) model that is fully consisted with the symmetry constraints discussed above. The active orbits are the two local  $d_{z^2}$  states centered on the Ta atoms, and they provide the four local basis states when spin degree of freedom is included. Four hopping parameters are given to describe the  $d_{z^2}$  bands near the Fermi surface, and their definitions are presented in Fig. 6(a) schematically. The two types of Ta atoms are denoted by triangles with different orientations. The hopping process along the TaS<sub>3</sub> chains is denoted by  $t_z$ . In the  $x$ - $y$  plane, the hopping process taking place in the same Ta sublattice is defined as  $t_{xy}$  while the hopping between different sublattices in the slant direction is defined as  $t_{xy}^{ab}$ . There are also spin-dependent hoppings when the spin orbit coupling is taken into consideration.

With these hopping parameters we are able to construct a  $4 \times 4$  Hamiltonian  $H_{TB}(\mathbf{k})$  as

$$H_{TB}(\mathbf{k}) = \begin{bmatrix} g(\mathbf{k}) & u(\mathbf{k}) + v(\mathbf{k}) & 0 & 0 \\ & g(\mathbf{k}) & 0 & 0 \\ \dagger & & g(\mathbf{k}) & u^*(\mathbf{k}) + v^*(\mathbf{k}) \\ & & & g(\mathbf{k}) \end{bmatrix}, \quad (\text{C1})$$

where

$$\begin{aligned} g(\mathbf{k}) &= 2t_{xy}[\cos \mathbf{k} \cdot \mathbf{a} + \cos \mathbf{k} \cdot \mathbf{b} + \cos \mathbf{k} \cdot (\mathbf{a} + \mathbf{b})] \\ &= 2t_{xy} \left[ 2 \cos \frac{k_x a_0}{2} \cos \frac{\sqrt{3}k_y a_0}{2} + \cos k_x a_0 \right], \end{aligned}$$

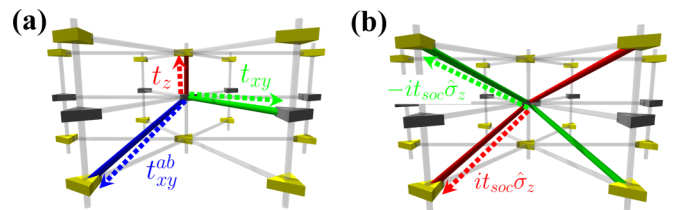


FIG. 6. Hopping parameters of the tight-binding model for the (a) spin-independent and (b) spin-dependent hopping processes. The gray and golden triangles denote the two orbits of the model, and the bonds linking them represent the corresponding hopping parameters.



$$\begin{aligned}
 v(\mathbf{k}) &= 2it_{\text{soc}} \sin \frac{\mathbf{k}_z \cdot \mathbf{c}}{2} [\sin \mathbf{k} \cdot \mathbf{a} + \sin \mathbf{k} \cdot \mathbf{b} - \sin \mathbf{k} \cdot (\mathbf{a} + \mathbf{b})] \\
 &= 2it_{\text{soc}} \sin \frac{k_z c}{2} \left[ 2 \sin \frac{k_x a_0}{2} \cos \frac{\sqrt{3}k_y a_0}{2} - \sin k_x a_0 \right], \\
 u(\mathbf{k}) &= t_{xy}^{ab} \cos \frac{\mathbf{k}_z \cdot \mathbf{c}}{2} [\cos \mathbf{k} \cdot \mathbf{a} + \cos \mathbf{k} \cdot \mathbf{b} + \cos \mathbf{k} \cdot (\mathbf{a} + \mathbf{b})] \\
 &\quad + 2t_z \cos \frac{\mathbf{k}_z \cdot \mathbf{c}}{2} \\
 &= 2t_{xy}^{ab} \cos \frac{k_z c}{2} \left[ 2 \cos \frac{k_x a_0}{2} \cos \frac{\sqrt{3}k_y a_0}{2} + \cos k_x a_0 \right] \\
 &\quad + 2t_z \cos \frac{k_z c}{2}, \tag{C2}
 \end{aligned}$$

with  $\hat{a} = (\frac{1}{2}, -\frac{\sqrt{3}}{2}, 0)a_0$  and  $\hat{b} = (\frac{1}{2}, \frac{\sqrt{3}}{2}, 0)a_0$ . Here  $a_0$  is the lattice constant in the  $x$ - $y$  plane. It is easily verified that, for high symmetry paths  $k_x = 0$  and  $k_x = \pm\sqrt{3}k_y$  on the  $k_z = \pi/c$  plane,  $u(\mathbf{k}) = v(\mathbf{k}) = 0$ , indicating that there exist three node lines.

We also fit the *ab initio* band structure shown in the main text with this TB model, and the results are shown in Fig. 7. With suitable parameters, the *ab initio* band structures are fitted qualitatively well. As the *ab initio* band structures are strongly

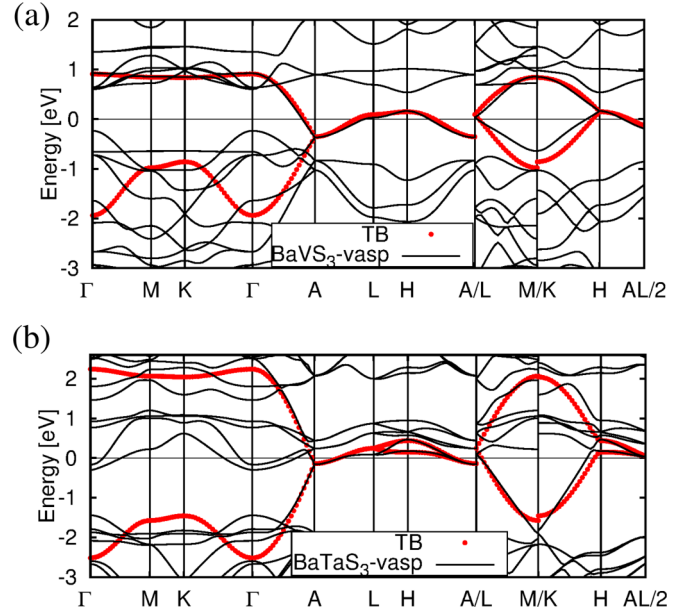


FIG. 7. Fitting of the *ab initio* band structure by the tight-binding model for the spinless case of BaVS<sub>3</sub> (top) and the spinful case of BaTaS<sub>3</sub> (bottom). Fitting parameters are  $t_z = -0.52$  eV,  $t_{xy}^{ab} = -0.032$  eV, and  $t_{xy} = -0.056$  eV for BaVS<sub>3</sub> and  $t_z = -0.90$  eV,  $t_{xy}^{ab} = -0.040$  eV,  $t_{xy} = -0.055$  eV, and  $t_{\text{soc}} = 0.062$  eV for BaTaS<sub>3</sub>.

hybridized to the other valence bands, we are more focused on the bands along the path A–L–H–A.

- [1] M. Z. Hasan and C. L. Kane, *Rev. Mod. Phys.* **82**, 3045 (2010).
- [2] X.-L. Qi and S.-C. Zhang, *Rev. Mod. Phys.* **83**, 1057 (2011).
- [3] H. Weng, C. Fang, Z. Fang, B. A. Bernevig, and X. Dai, *Phys. Rev. X* **05**, 011029 (2015).
- [4] S.-Y. Xu, C. Liu, S. K. Kushwaha, R. Sankar, J. W. Krizan, I. Belopolski, M. Neupane, G. Bian, N. Alidoust, T.-R. Chang, H.-T. Jeng, C.-Y. Huang, W.-F. Tsai, H. Lin, P. P. Shibayev, F.-C. Chou, R. J. Cava, and M. Z. Hasan, *Science* **347**, 294 (2015).
- [5] B. Q. Lv, H. M. Weng, B. B. Fu, X. P. Wang, H. Miao, J. Ma, P. Richard, X. C. Huang, L. X. Zhao, G. F. Chen, Z. Fang, X. Dai, T. Qian, and H. Ding, *Phys. Rev. X* **5**, 031013 (2015).
- [6] X. Wan, A. M. Turner, A. Vishwanath, and S. Y. Savrasov, *Phys. Rev. B* **83**, 205101 (2011).
- [7] T. T. Heikkilä, N. B. Kopnin, and G. E. Volovik, *JETP Lett.* **94**, 233 (2010).
- [8] T. T. Heikkilä and G. E. Volovik, *JETP Lett.* **93**, 59 (2011).
- [9] T. T. Heikkilä and G. E. Volovik, *New J. Phys.* **17**, 093019 (2015).
- [10] C. Fang, Y. Chen, H.-Y. Kee, and L. Fu, *Phys. Rev. B* **92**, 081201 (2015).
- [11] C. Fang, L. Lu, J. Liu, and L. Fu, *arXiv:1512.01552*.
- [12] H. Weng, Y. Liang, Q. Xu, R. Yu, Z. Fang, X. Dai, and Y. Kawazoe, *Phys. Rev. B* **92**, 045108 (2015).
- [13] Y. Kim, B. J. Wieder, C. L. Kane, and A. M. Rappe, *Phys. Rev. Lett.* **115**, 036806 (2015).
- [14] R. Yu, H. Weng, Z. Fang, X. Dai, and X. Hu, *Phys. Rev. Lett.* **115**, 036807 (2015).
- [15] L. S. Xie, L. M. Schoop, E. M. Seibel, Q. D. Gibson, W. Xie, and R. J. Cava, *APL Mater.* **3**, 083602 (2015).
- [16] G. Bian, T.-R. Chang, R. Sankar, S.-Y. Xu, H. Zheng, T. Neupert, C.-K. Chiu, S.-M. Huang, G. Chang, I. Belopolski, D. S. Sanchez, M. Neupane, N. Alidoust, C. Liu, B. Wang, C.-C. Lee, H.-T. Jeng, C. Zhang, Z. Yuan, S. Jia, A. Bansil, F. Chou, H. Lin, and M. Z. Hasan, *Nat. Commun.* **7**, 10556 (2016).
- [17] M. Phillips and V. Aji, *Phys. Rev. B* **90**, 115111 (2014).
- [18] T. T. Heikkilä and G. E. Volovik, *arXiv:1504.05824*.
- [19] A. A. Burkov and L. Balents, *Phys. Rev. Lett.* **107**, 127205 (2011).
- [20] R. A. Gardner, M. Vlasse, and A. Wold, *Acta Crystallogr., Sect. B* **25**, 781 (1969).
- [21] R. A. Gardner, M. Vlasse, and A. Wold, *Inorg. Chem.* **8**, 2784 (1969).
- [22] G. Kresse and J. Furthmüller, *Phys. Rev. B* **54**, 11169 (1996).
- [23] J. P. Perdew, K. Burke, and M. Ernzerhof, *Phys. Rev. Lett.* **77**, 3865 (1996).
- [24] P. E. Blöchl, *Phys. Rev. B* **50**, 17953 (1994).
- [25] S. L. Dudarev, G. A. Botton, S. Y. Savrasov, C. J. Humphreys, and A. P. Sutton, *Phys. Rev. B* **57**, 1505 (1998).
- [26] N. Marzari, A. A. Mostofi, J. R. Yates, I. Souza, and D. Vanderbilt, *Rev. Mod. Phys.* **84**, 1419 (2012).
- [27] S. A. Parameswaran, A. M. Turner, D. P. Arovas, and A. Vishwanath, *Nat. Phys.* **9**, 299 (2013).
- [28] A. König and N. D. Mermin, *Phys. Rev. B* **56**, 13607 (1997).

- [29] Q. D. Gibson, L. M. Schoop, L. Muechler, L. S. Xie, M. Hirschberger, N. P. Ong, R. Car, and R. J. Cava, *Phys. Rev. B* **91**, 205128 (2015).
- [30] L. F. Mattheiss, *Solid State Commun.* **93**, 791 (1995).
- [31] M. H. Whangbo, H. J. Koo, D. Dai, and A. Villesuzanne, *J. Solid State Chem.* **165**, 345 (2002).
- [32] X. Jiang and G. Y. Guo, *Phys. Rev. B* **70**, 035110 (2004).
- [33] P. C. Donohue and J. F. Weiher, *J. Solid State Chem.* **10**, 142 (1974).
- [34] T. Ohtani, H. Sawada, and M. Chikamori, *Mater. Res. Bull.* **39**, 561 (2004).